

Synthesis of porous nanostructured MoS₂ materials in thermal shock conditions and their performance in lithium-ion batteries

**Svetlana G. Stolyarova,¹ Alena A. Kotsun,¹ Yury V. Shubin,¹ Victor O. Koroteev,² Pavel E. Plyusnin,¹ Yury L. Mikhlin³, Maxim S. Mel'gunov⁴, Alexander V. Okotrub,¹ Lyubov G. Bulusheva¹*

¹Nikolaev Institute of Inorganic Chemistry SB RAS, 3 Acad. Lavrentiev Ave., 630090 Novosibirsk, Russia

²CIC nanoGUNE BRTA, Tolosa Hiribidea 76, E-20018 Donostia - San Sebastian, Spain

³Institute of Chemistry and Technology, Krasnoyarsk Science Center of the Siberian Branch of the Russian Academy of Sciences, 50/24 Akademgorodok, 660036 Krasnoyarsk, Russia

⁴Boreskov Institute of Catalysis SB RAS, 5 Acad. Lavrentiev Ave., 630090 Novosibirsk, Russia

*corresponding author: stolyarova@niic.nsc.ru

Abstract

We offer a simple synthesis of porous nanostructured MoS₂ materials by the rapid decomposition of ammonium tetrathiomolybdate aerogel in an inert atmosphere at temperatures of 400–700°C. The synthesis products consist of thin elongated porous plates where pores 2–30 nm in size are surrounded by curved MoS₂ layers. The temperature gradient arising upon the heating leads to the creation of the extended MoS₂ layers on the surface of the plates. The lateral size and the number of adjacent layers on the surface and inside the plates increase with the synthesis temperature. The material obtained at 700°C showed the best rate capability in lithium-ion batteries. Its specific

capacity was 817 mAh g⁻¹ at a current density of 2 A g⁻¹ and reached 1139 mAh g⁻¹ in subsequent cycling at 0.1 A g⁻¹. Electrochemical impedance spectroscopy revealed fast diffusion of lithium ions and low resistance of charge transfer for this material. A unique architecture, where the hard shell prevents the loss of electrochemically active species and the conductive intertwined MoS₂ layers preserve pores for the accommodation of these species, provides a high stability and large storage capacity of the material. The developed synthetic technique can be adopted for nanostructuring of other redox-active compounds promising for energy application fields.

Keywords: ammonium tetrathiomolybdate, thermal shock, porous MoS₂, nanostructuring, lithium-ion battery

1. Introduction

Lithium-ion batteries have firmly entered the life of human society, providing autonomous power supply for various portable devices (smartphones, laptops, headphones, etc.) and high-power devices (buses, metro, electric motors, etc.)¹⁻⁴. The improvement of these devices and the development of new ones demand batteries of greater capacity, power, and longer battery life. These characteristics are determined by battery components, mostly by anode and cathode material. Current research in the field of anode materials is aimed to finding an alternative to graphite used in commercial lithium-ion batteries⁵⁻⁷. MoS₂ is actively explored as a promising anode material. Layered MoS₂ can accumulate lithium owing to two electrochemical processes^{1,8}. Firstly, lithium ions intercalate into the interlayer spaces at a potential from 3 to 1.1 V vs. Li/Li⁺. The second process involves the conversion of the intercalate Li_xMoS₂ at ~ 0.6 V with the formation of Mo and Li₂S. The theoretical specific capacity provided by the intercalation and conversion reactions is 669 mAh g⁻¹, which is 1.8 times higher than the corresponding value for graphite.

The main disadvantage of bulk MoS₂ as an anode material is the short battery life. This is explained by the strong deformation of the lattice of the MoS₂ crystal and an increase in its volume by 15–20% upon the intercalation of lithium ions⁹. The MoS₂-based material can be stabilized by

carbon component that provides the conductivity of the composite, compensates the increase in the volume of the MoS₂ lattice, and prevents the diffusion of sulfur species from the anode^{6,10–12}. An alternative approach is to obtain nanostructured MoS₂¹³. A decrease in the number of layers increases the electrical conductivity of MoS₂¹⁴, while small lateral particle size and enlarged interlayer distance damp down the change in the volume of the material during cycling of the battery. The synthesis of MoS₂ nanoparticles creates defects in the lattice (mainly grain boundaries, heteroatom-doping), which serve as additional centers of lithium adsorption and can accelerate the diffusion of lithium ions^{15,16}.

It has been shown that the reversible capacity of nanostructured MoS₂ materials can reach 800–1200 mAh g⁻¹^{17–19}, significantly exceeding the value of the theoretical capacity of the hexagonal MoS₂. Ex situ and in situ studies of electrode materials after extraction of lithium find sulfur instead of the MoS₂ phase^{20,21}. This observation indicates that the conversion reaction of MoS₂ is irreversible. The theoretical capacity of the electrochemical reaction of elemental sulfur with lithium ions is 1675 mAh g⁻¹, and the occurrence of this reaction can explain the high values of capacity observed for MoS₂ in lithium-ion batteries, which, starting from the second cycle, actually work as Li-S batteries. The problem of Li-S batteries is a low conductivity of lithium polysulfides, formed during the battery operation, and their dissolution in organic electrolytes which leads to the loss of active material and a rapid drop in capacity²². In the case of MoS₂, it is assumed that the metallic molybdenum resulting from the conversion reaction ensures the conductivity of the electrode material and stabilizes it due to the coordination of sulfur atoms around the Mo clusters¹⁷.

Other experimental data demonstrate the preservation of MoS₂ layers after several tens of full charge/discharge cycles of the battery^{19,23–25} and reversibility of the electrochemical reaction between Mo and Li₂S²⁶. The fast kinetics of the process in such materials is associated with a high mobility of lithium ions in the expanded interlayer space of stable MoS₂ layers or the formation of new paths of lithium diffusion^{13,27,28}. Examples of stable MoS₂ structures, where intercalation

reactions are maintained during repeating insertion/extraction of lithium ions, are layers perpendicular to the substrate surface ²⁷, porous tubular structures ²⁸, nanobelts ²⁹, materials with ordered mesopores ³⁰ and hollow spheres ³¹. Syntheses of these materials use approaches of self-organization of particles in solutions and growth on templates. However, electrochemical studies in these cases also reveal reactions between sulfur and lithium ions, which make the main contribution to the superior capacity of the MoS₂-based anode. The presence in the literature of various points of view on the mechanism of the electrochemical behavior of MoS₂ in lithium-ion batteries requires additional research in this area.

In this work, we proposed and realized a simple method for the synthesis of porous nanostructured MoS₂ materials as a result of rapid heating of ammonium tetrathiomolybdate (ATM) (NH₄)₂MoS₄. The method of thermal shock is widely used to obtain thin graphene layers from graphite compounds ³²⁻³⁴. The exfoliation of the compounds with covalent bonds, such as graphite oxide or graphite fluoride, leads to the synthesis of wrinkled layers with a large number of vacancy defects ^{35,36}. ATM is an ideal candidate for the synthesis of MoS₂ under conditions of thermal shock because it contains both sulfur and molybdenum. Previous works on the preparation of MoS₂ from ATM powders and films were based on long heat treatment procedures with slow heating to the desired temperature ^{37,38}. Such procedures minimize the number of defects and edge states, leading to good crystallization of MoS₂. In our case, the use of aerogel provides a high dispersion of the initial ATM, which is important for the quick removal of gaseous decomposition species from the synthesis product. A short synthesis time ensures the formation of MoS₂ nanoparticles, and the high pressure created by the released gases leads to their strong bonding with the formation of a porous architecture of the material. The determining factor affecting the structure of the materials obtained in this process is the synthesis temperature.

The present paper aims to study the relationships between the structure of MoS₂ materials synthesized at different ATM decomposition temperatures and their electrochemical behavior in lithium-ion batteries. The structure and composition of the materials were investigated by electron

microscopy, X-ray diffraction (XRD) analysis, Raman spectroscopy, elemental analysis, and X-ray photoelectron spectroscopy (XPS). Electrochemical properties were tested in the galvanostatic mode, by cyclic voltammetry (CV) and electrochemical impedance spectroscopy (EIS). The materials produced without using a carbon component in the synthesis showed a reversible specific capacity of up to 1139 mAh g⁻¹ and they can be considered as a candidate for Na- and K-ion batteries.

2. Materials and methods

2.1. Synthesis

ATM was synthesized by passing H₂S (99.5%) through an ammonia solution (60 mL) of ammonium heptamolybdate tetrahydrate (NH₄)₆Mo₇O₂₄·4H₂O (5 g) for 4 h. Obtained crystals were collected on a glass filter, washed with a cold solution of ethanol, and dried in air. A portion of ATM crystals (1.5 g) was dissolved in distilled water (150 mL) and the solution was subjected to freeze-drying.

The synthesis of molybdenum (IV) disulfide was carried out in a vertical tubular quartz reactor in a constant flow (7.5 mL/s) of pure argon (99.998%). The reactor was heated to the required temperature (400, 500, 600, or 700 °C) and ATM aerogel was immersed there for 10 sec. Then the reactor was removed from the furnace and naturally cooled to room temperature in 15 min. The samples synthesized at 400, 500, 600, and 700 °C, are denoted below by ATM400, ATM500, ATM600, and ATM700, respectively.

2.2. Characterization methods

Infrared (IR) spectrum of ATM aerogel was measured on a Fourier-transform Scimitar FTS–2000 spectrometer. Simultaneous thermal analysis (STA) of the aerogel included thermogravimetric (TG), differential scanning calorimetry (DSC), and evolved gas analysis using mass spectrometry (EGA-MS). The measurements were performed on a NETZSCH STA 449A1cc Jupiter® instrument combined with a quadrupole mass spectrometer QMS 403D Aëolos®. The sample was

placed in an open Al₂O₃ crucible and heated in a helium flow (30 mL/min) from room temperature to 800 °C at a rate of 10 °C min⁻¹. An electronic impact ionizer operated at an energy of 70 eV. Ion currents of the selected mass/charge (m/z) numbers were monitored in multiple ion detection mode with a collection time of 1 s for each channel. Processing of experimental data was carried out using a standard software package Proteus analysis³⁹.

Morphology and structure of MoS₂ samples were investigated by scanning electron microscopy (SEM) on a FEI Helios 450S dualbeam FIB/SEM microscope and transmission electron microscopy (TEM) on a Jeol 2010 microscope.

XRD of the samples was carried out on a Shimadzu XRD-7000 diffractometer (Cu K α radiation, Ni filter on the reflected beam). After electrochemical cycling, ex situ XRD was performed for electrodes (materials on copper foils) removed from the cell, washed in diethyl carbonate, and dried in vacuum. The measurements were done for the samples of approximately the same mass and under identical experimental conditions.

Raman spectra were recorded on a LabRAM HR Evolutiona (Horiba) spectrometer using an Ar⁺ laser line ($\lambda = 488$ nm) at a power of 1 mW. The diameter of the laser spot was 2 μ m.

Brunauer–Emmett–Teller (BET) surface areas were calculated using nitrogen adsorption data at –196 °C obtained on a Quantachrome QuadroSorb Evo instrument. The total pore volume was estimated from the uptake of nitrogen at a partial pressure of 0.98.

Elemental composition of samples we determined on a vario MICRO cube CHNS-analyzer. An analyzed sample was decomposed in oxygen (99.995%) at a temperature of 1150 °C in the presence of a WO₃ catalyst. The resulting mixture of gases (CO₂, H₂O, N₂, SO₂) was separated on a chromatograph using a thermal conductivity detector. The carrier gas was helium (99.995%).

The surface composition of MoS₂ samples and electronic state of the elements were studied by XPS with a SPECS photoelectron spectrometer equipped with a PHOIBOS 150 MCD9 energy analyzer at electron take-off angle 90° using monochromatic Al K α radiation (1486.7 eV). The residual gas pressure in the analytical chamber of the spectrometer was 10⁻⁹ mbar. The processing

of the spectra was carried out using CasaXPS software. The elemental composition was determined from the survey XPS spectra; the high-resolution spectra were fitted using Gaussian-Lorentzian peak profiles after subtraction of Shirley type background.

1.3. Electrochemical measurements

To prepare the working electrode, the testing material (~30 mg), conductive additive (super P), and polyvinylidene fluoride were taken in a weight ratio of 8:1:1 and mixed with N-methyl-2-pyrrolidone (NMP). The obtained suspension was applied on copper foil and dried at 60 °C for 12 h in vacuum. Coin cells of CR2032 type were assembled with lithium metal as the counter electrode in a glove box filled with argon. The electrolyte was 1 M solution of LiPF₆ in a mixture of ethylene carbonate and dimethyl carbonate (1:1 by volume) from Merck Co. Galvanostatic charge/discharge cycles were recorded at NEWARE CT-3008 stations from 0.01 to 2.50 V at current densities from 0.1 A g⁻¹ to 2 A g⁻¹. CV and EIS studies were performed on a Bio-Logic SP-300 station for the cycled cells in a range of potentials of 0.01–3.0 V relative to Li/Li⁺ and frequencies of 0.01–1 MHz, respectively.

3. Results

3.1 Materials characterization

The synthesis of nanostructured MoS₂ materials is illustrated in Fig. 1a. An aqueous solution containing freshly prepared ATM in a concentration of ~1 wt% has a dark-brown color. Freeze-drying of the solution leads to the formation of an orange ATM aerogel. A study of the aerogel by IR-spectroscopy confirmed the formation of Mo–S and N–H bonds (Fig. S1) characteristic of (NH₄)₂MoS₄⁴⁰. The vibrations observed in the regions of 3300–3660, 2690–3000, and 1420–1680 cm⁻¹ indicate incomplete removal of solvent (H₂O and C₂H₅OH) from the aerogel⁴¹. Rapid heating of ATM in an argon atmosphere yields black product (Fig. 1a).

The decomposition process of ATM aerogel was studied in helium by the STA (Fig. 1b). TG curve showed two plateaus in agreement with earlier studies on the thermal decomposition of

$(\text{NH}_4)_2\text{MoS}_4$ powders and films^{37,42–44}. The first step is a conversion of $(\text{NH}_4)_2\text{MoS}_4$ to MoS_3 according to $(\text{NH}_4)_2\text{MoS}_4 \rightarrow \text{MoS}_3 + 2\text{NH}_3\uparrow + \text{H}_2\text{S}\uparrow$, as ion currents with the m/z values of 14, 15 and 34 characteristics for NH_3 and H_2S indicate. This endothermic process in our case occurs in the range of 120–220 °C, where the upper temperature is slightly lower than that for crystalline samples^{43–45}. In this range the ion currents corresponding to SO and SO_2 (m/z equal to 48 and 64, respectively) appear, indicating oxidation of sulfur by oxygen species remaining in the aerogel. The decomposition of trapped ethanol molecules is accompanied by the currents with the m/z values of 31, 45, 29, 27, and 46 (Fig. S2). The second plateau observed in the TG curve of ATM from 300 to 600 °C corresponds to the reaction: $\text{MoS}_3 \rightarrow \text{MoS}_2 + \text{S}\uparrow$. The DSC curve shows an exothermic peak for this reaction, which has been assigned to the crystallization of disulfide particles³⁷. At temperatures above 700 °C TG and DTG curves do not show significant mass changes.

Based on the STA data, we chose the temperature range for the synthesis from 400 °C, when the formation of MoS_2 occurs, to 700 °C. Table 1 presents the estimated composition of ATM decomposition products obtained using the TG data at the selected temperatures. The decomposition should lead to the synthesis of sulfur-enriched and sulfur-deficient MoS_2 at temperatures below and above 600°C, respectively.

SEM examination of the synthesis products did not reveal any obvious difference in their morphologies (Fig. S3). Rapid decomposition of ATM produces elongated plates of different sizes regardless of the synthesis temperature. Typical SEM images obtained at low and high magnifications are shown in Fig. 2a,b. The average length and width of the plates are 0.7 μm and 4 μm , respectively. At a larger magnification, it can be seen that the surface of the plates is not smooth, and the images from the ends of the plates demonstrate their porosity (Fig. 2b). Low-resolution TEM image of ATM700 taken as an example shows many bright spots corresponding to pores of 2–30 nm (Fig. 2c).

High-resolution TEM images of the samples are compared in Fig. 2d-g. The structure of ATM400 is amorphous-like (Fig. 2e), whereas ATM500 contains MoS₂ nanocrystals with a lateral size of 3–7 nm and the number of layers from 2 to 4 (Fig. 2f). The rise of the synthesis temperature to 700 °C led to the formation of extended layers on the surface of plates (Fig. 2h). However, the plate interior contains short nanocrystals of 4 curved MoS₂ layers mainly. The layers of individual neighboring particles intertwine forming an onion-like structure around the cavity. The distance between the MoS₂ layers in all samples is ~0.66 nm, which is close to the value characteristic of bulk MoS₂ (0.62 nm).

Adsorption/desorption of N₂ was measured for ATM600 obtained at 600 °C. The BET specific surface of the sample is 57 m² g⁻¹, which is ~16 times greater than the value for bulk MoS₂ (~3.7 m² g⁻¹). The pore size varies from 2 to 35 nm with a prevalence of 4–5 nm (Fig. S4). The total pore volume is 0.1 cm³ g⁻¹.

XRD patterns exhibited the (002) reflection of hexagonal MoS₂ for all samples (Fig. 3a). The absence of (100), (103), and (110) reflections in the pattern of ATM400 is probably due to the very small lateral size of the MoS₂ layers. These reflections are broadened for ATM500 and ATM600 and become narrower in the case of ATM700, where bigger MoS₂ layers are observed by TEM (Fig. 2h). The interlayer distance and the number of layers in MoS₂ nanoparticles were calculated from correspondingly position and broadening of the (002) reflection (Table 2). The average distance between the MoS₂ layers is 0.63 nm. An increase in the synthesis temperature led to growing the number of layers from 3 in ATM400 to 7 in ATM700.

Raman spectra of the samples showed peaks at 380 and 404 cm⁻¹ (Fig. 3b) corresponding to the E_{2g}¹ and A_{1g} modes of atomic vibrations along the S–Mo–S bonds and perpendicular to them, respectively⁴⁶. The distance between the peaks Δ depends on the number of layers of MoS₂⁴⁷. However, this value is constant in the set of the samples, and the positions of the peaks E_{2g}¹ and A_{1g} are shifted by 3–7 cm⁻¹ relative to the corresponding values for bulk MoS₂ samples (383 and 408 cm⁻¹)⁴⁸. Such behavior of Raman scattering⁴⁸ is due to the curvature of MoS₂ layers⁴⁹ in

correspondence with the TEM observation (Fig. 2f–h). A decrease in the width of the peaks from ATM400 to ATM700 indicates an increase in the crystallinity and order of the formed MoS₂ layers and this agrees with the TEM and XRD data.

Survey XPS spectra of the samples showed signals from S, Mo, O, and C (Fig. S5); surface concentrations of elements are given in Table S1. The contents of carbon and oxygen are 29–47 and 12–24 at.%, respectively. The carbon component was formed by the pyrolysis of ethanol, which has been used at the stage of washing the synthesis products. According to the CHNS analysis, however, the samples contain no more than ~2 at% of carbon (Table S2). Therefore, carbon is localized on the surface of the plates. TEM images of the samples show a thin surface coating that has less contrast than MoS₂ layers, shown by arrows in Figs. 2g, h. CHNS analysis also detects traces of nitrogen in the samples in amounts of less than 2 at.%.

XPS S 2p spectra of the samples were described by spin-orbit S 2p_{3/2-1/2} doublets with the splitting of 1.2 eV (Fig. 3c). The component with the S 2p_{3/2} binding energy of 161.9 eV corresponds to the S²⁻ states in MoS₂⁵⁰, and the high-energy doublet at 163.2 eV can be assigned to elemental sulfur S⁰ or bridging groups S₂²⁻ on the edges of MoS₂ particles^{51,52}. A small amount of the oxidized sulfur species was found in ATM400 and ATM600. In the sequence of samples from ATM400 to ATM700, the fraction of S⁰ and/or S₂²⁻ species decreases from 44% to less than 0.3% (detection limit of XPS) which correlates with the STA data showing sulfur removal with the temperature.

XPS Mo 3d_{5/2-3/2} spectra (Fig. S6a) were fitted with two spin-orbit doublets corresponding to Mo⁴⁺ state in MoS₂ with the Mo 3d_{5/2} binding energy of 229.2 eV and oxidized forms of molybdenum (weak doublet with Mo 3d_{5/2} peak at 233.5 eV). The fraction of oxidized molybdenum was 14.4 % in ATM400 and did not exceed 3.9 % in other samples. The width of the Mo⁴⁺ components decreased with the synthesis temperature, which confirms the improvement of the atomic ordering of MoS₂.

Fig. 3d shows models of MoS₂ layers for compositions calculated using the TG data (Table 1). Excess sulfur in ATM400 and ATM500 can be provided by bridging S₂²⁻ groups. In sample ATM600 with a composition close to MoS₂, the S:Mo ratio at the edges of the layers is 1:1. The Mo-terminated edges should predominate in the sulfur-deficient ATM700 sample. The prevalence of such edges might explain the lower S:Mo values determined from XPS as compared to those estimated from TG data ⁵³.

XPS C 1s spectra of the samples exhibited an intense peak at 284.7 eV and a peak at 288.9 eV (Fig. S6b). The position of the main peak is shifted toward higher binding energy relative to the value of 284.5 eV specific for graphite. The reason may be the bonding of some carbon atoms with electronegative oxygen and/or the curvature and defectiveness of graphene layers with small lateral size ⁵⁴. All spectra show a high-energy component at ~289 eV from carboxyl groups ⁵⁵ and a component at 286.2 eV from carbon bonded with hydroxyl ⁵⁶. The area of high-energy components is about 20%; therefore, oxygen is mostly associated with carbon on the surface of MoS₂-based plates. The oxidized species are most likely formed due to the contact of samples with air. Spectra of samples ATM500, ATM600, and ATM700 also showed a component at 283.8 eV related to carbon atoms at the boundary of graphene fragments ⁵⁷. The intensity of this component increased with increasing temperature of the sample synthesis.

3.2 Electrochemical tests

The curves for the first three discharge-charge cycles measured for MoS₂ samples at a current density of 0.1 A g⁻¹ are presented in Figs. 4a–d. At first insertion of lithium ions in the electrode, all discharge curves show two plateaus at 1.3–1.2 and 0.8–0.6 V due to the intercalation of the ions between MoS₂ layers and the conversion of the intercalate to metallic Mo and Li₂S, respectively ¹. Also, the curves of ATM400 and ATM500 have a plateau at ~1.9 V assigned to the reaction of sulfur with lithium ions. Analysis of TG data of ATM aerogel predicts excess sulfur in these samples relative to ideal MoS₂ composition (Table 1). The S 2p spectra of the samples have a significant intensity of the high-energy component related to elemental sulfur or boundary S₂²⁻

bridge pairs. Sample ATM400 had the highest irreversible capacity ($\sim 290 \text{ mAh g}^{-1}$) associated mainly with the formation of solid electrolyte interphase (SEI) film. For other samples, this value did not exceed $\sim 220 \text{ mAh g}^{-1}$. After the first full discharge-charge cycle, the specific capacity decreases in the sequence of samples ATM600>ATM400>ATM500>ATM700. Starting from the second cycle of the cell operation, the discharge curves of all samples show a plateau at $\sim 2.0 \text{ V}$, whose length decreases with the increase of MoS₂ synthesis temperature. In the samples synthesized at temperatures above 400 °C the second and third discharge curves have a plateau at 1.1 V assigned to the intercalation of lithium ions between MoS₂ layers.

The curves for the second and third discharge or charge of the cells are almost identical, showing significant changes in the structure of MoS₂ during the first cycle only. Therefore, the EIS study was performed for electrode materials after the first full discharge-charge cycle. The Nyquist plots of the impedance spectra start with a semicircle in the high-frequency region (Fig. S7) corresponding to the resistance of the SEI film and the contact resistance (R_f)⁵⁸. The second semicircle is assigned to charge transfer resistance (R_d) and a straight line in the low-frequency region (Fig. 4e) is related to the diffusion of lithium ions in the electrode material. A larger angle between this line and the $\text{Re}(Z)$ axis means a higher diffusion rate of the ions. The resistance values were determined by fitting the impedance spectra by an equivalent circuit shown in Fig. S7. The greatest contact resistance R_f was found for the ATM700 electrode in consistence with a larger number of layers and better atomic ordering of MoS₂ in this sample. However, the electrode possessed the smallest value of charge transfer resistance R_d (Fig. S7). The higher electrical conductivity of the material can be provided by Mo-terminated MoS₂ layers (Fig. 3d), as quantum-chemical calculations predict^{18,59}. The largest slope angles of the straight lines equal to 61.9 and 57.9° were determined from the spectra of ATM400 and ATM700, respectively (Fig. 4e). The high rate of ion diffusion in these samples could be due to a very small size of MoS₂ layers in ATM400 and a high degree of MoS₂ ordering in ATM700.

Capacity measurements of the samples at current densities of 0.1, 0.5, 1, and 2 Ag^{-1} confirmed the EIS data, which determined the ATM700 as the sample with best electrochemical performance. Among the investigated materials this sample showed the highest values of specific capacity of 874 and 817 mAh g^{-1} at 1 and 2 Ag^{-1} , respectively (Fig. 4f). The specific capacity measured at 2 Ag^{-1} for ATM600, ATM400, and ATM500 was equal to 558, 440, and 316 mAh g^{-1} respectively. At high current densities, the capacity of the material is determined by access to the electrochemically active species for lithium ions. Charge-discharge curves measured for ATM700 at a current density of 2 Ag^{-1} showed a large plateau around 2 V (Fig.S8). The corresponding reaction of sulfur with lithium ions provides about 50% of the total sample capacity. Easy availability of sulfur for lithium ions can be provided by the porosity of the material.

To determine the structural changes in the samples after the electrochemical interaction with lithium ions, ex situ XRD measurements were carried out for electrode materials after the fourth full cycles of cell operation at 0.1 A g^{-1} . We investigated ATM600 and ATM700 which showed the best kinetics of the process (Fig. 4f). To prevent materials from interaction with atmospheric oxygen, the cycled electrode was covered with a polyfluoroethylene (PTFE) film. Fig. 5a compares the XRD patterns of ATM600 electrode material before and after the cycling. A small amount of active material on copper foil allowed to register the (002) MoS_2 reflection only. Signals from the binder, PTFE, and copper prevail in the cycled sample. At small 2Θ angles, a weak peak is observed. The enlarged fragment of the pattern allows us to determine the position of this peak at $2\Theta=9.2^\circ$ (Fig. 5b) which corresponds to the interlayer distance of 0.96 nm. After cycling of ATM700, the (002) reflection also shifted to smaller angles (Fig. 5c). In this case, the interlayer distance increased to 1.0 nm which significantly exceeds the values of ~ 0.64 nm registered in several works for Li_xMoS_2 and MoS_2 after the cycling in lithium-ion batteries^{8,21,24}. In our material, the layers significantly expanded after lithiation which also provides better ion diffusion in subsequent cycles of the battery operation.

After a load of 2 A g^{-1} , the electrochemical testing of the cells was continued at 0.1 A g^{-1} (Fig. 4f). ATM700 electrode showed an increase of specific capacity to 1139 mAh g^{-1} as compared to the value of 888 mAh g^{-1} achieved at the first measurement cycles at this current density. The capacity of ATM600 returned to the previous value, whereas ATM400 and ATM500 showed a decrease in the capacity. CV was used to study the processes occurring in studied materials after 60 cycles of the operation of batteries. The CV curves revealed that the processes in all studied materials are dominated by electrochemical reactions between sulfur and lithium ions at oxidation/reduction potentials of $1.9\text{--}2.1/2.3\text{--}2.6 \text{ V}$ (Fig. 6a–d). Long-chain lithium polysulfides Li_2S_8 , Li_2S_6 are formed at lower potentials, while larger energy is required to produce Li_2S_2 and Li_2S ⁶⁰. The peaks at 2.3, 2.5, and 2.6 V are attributed to the reduction of polysulfides to Li_2S_6 , S, and S_8 , respectively²². The oxidation peaks at 1.19 and 0.41 V observed in the CV curves of ATM700 (Fig. 6d) can be attributed to the intercalation of lithium ions between the MoS_2 layers and the interaction of molybdenum clusters with lithium, respectively⁶¹. The reduction peak at 1.7 V corresponds to the delithination of Li_xMoS_2 ¹. Thus, even after several tens of discharge-charge cycles, ATM700, synthesized at $700 \text{ }^\circ\text{C}$, is a mixture of layered MoS_2 and Li_2S . The CV curves of the samples synthesized at lower temperatures showed a shift of the peak associated with the oxidation of molybdenum to potentials of $1.91\text{--}1.95 \text{ V}$ (Fig. 6a–c). A higher oxidation potential may indicate the formation of MoS_3 ^{62,63} at the delithination of the electrode materials. A large area of the corresponding peak in the CV curves of ATM400 (Fig. 6a), enriched with the sulfur, confirms this assumption. The interaction of MoS_3 with lithium ions is accompanied by the peaks at 1.4 and 0.35 V. A shift of these peaks in the CV curves of ATM500 and ATM600 (Fig. 6 b, c) may be due to a change in the chemistry of the process with lower sulfur content in the sample.

Kinetics of electrochemical processes that occurred in MoS_2 materials were studied for the best sample ATM700. Fig. 6e presents CV curves measured at various scan rates of potential. The current i provided by the redox process depends on the scan rate ν according to the power law $i(\nu) = a\nu^b$ ^{64,65}. A b -value of 1 indicates a capacitive process and a value of 0.5 indicates a diffusion-

controlled process. Fig. 6f shows the $\log(i)$ vs. $\log(v)$ dependences plotted for five redox peaks observed in the CV curve of ATM700 sample (Fig. 6e). The b -value of 1.1 determined for the peak R1 qualifies the reaction $nS+2Li^++2e^- \rightarrow Li_2S_n$ as exclusively capacitive. For all other reactions, this value does not exceed 0.8 and therefore both redox and diffusion processes contribute to the capacity.

3.3. Discussion

SEM study of the products of ATM thermolysis revealed no influence of the synthesis temperature on the sample morphology (Fig. S3). We suppose that the rapid heating of ATM aerogel determines the formation of specific thin elongated microscale plates. $(NH_4)_2MoS_4$ molecules decompose with the release of gases H_2S and NH_3 , which escape from the plates, making their surface rough. High pressure of the gaseous products developed under thermal shock conditions leads to the creation of pores inside the plates. However, the synthesis temperature affects the structure of the plates. High-resolution TEM images of the sample produced at $400^\circ C$ show that the plate interior is amorphous-like (Fig. 2d). An increase of the synthesis temperature to $500^\circ C$ provides the formation of few-layer MoS_2 nanocrystals with small lateral sizes (Fig. 2e). According to the XRD and Raman spectroscopy data, the crystallinity of the plates increases with the temperature. TEM examination of the samples indicated more extended and thick layers at the plate surface that could be related to the temperature gradient from the surface to the plate interior. The decomposition products of the organic solvent used in the production of aerogel and adsorbed on the surface of fine $(NH_4)_2MoS_4$ crystallites deposit on the plate surface as a thin graphene-like coating with a large number of edge defects.

The final temperature of $700^\circ C$ for the ATM thermolysis was chosen based on the TG analysis which detected almost no weight loss above this temperature. However, thermal shock conditions can modify the processes of ATM decomposition and MoS_2 crystallization. Electrochemical tests of the samples showed the highest values of specific capacity for ATM600 at initial discharge-charge cycles at a current density of $0.1 A g^{-1}$. The best rate capability was observed for ATM700

sample, moreover, the capacity of this sample increased as compared to the initial values when the current density was switched from 2 to 0.1 A g⁻¹ in contrast to the samples produced at lower temperatures (Fig. 4f). To be sure that the temperature of 700°C is optimal for our synthesis method, we have prepared the sample at 800°C. This sample gradually decreased capacity during cycling from 1219 to 460 mAh g⁻¹ at 0.1 A g⁻¹ and the capacity became very low at large current densities (Fig. S9a). Such capacitive behavior is characteristic of the bulk MoS₂⁵³. Thus we conclude that amount of surface defects required for penetration of lithium ions inside of the MoS₂ plate is low in the sample synthesized at 800°C. This conclusion is confirmed by examination of discharge-charge curves measured on the fortieth cycle of battery operation at 2 A g⁻¹, which showed no plateaus characteristic of redox reactions between sulfur and lithium ions (Fig. S9b).

The structure of MoS₂ material formed during the rapid thermolysis of ATM aerogel is schematically shown in Fig. 7a for ATM700 sample, demonstrated the best performance in lithium-ion batteries. Microscale plates have a hierarchical architecture with thin carbon skin covering extended MoS₂ layers and internal curved MoS₂ nanosheets, which intertwine to form pores. Defects and breakings in carbon coating and underlying MoS₂ layers allow easy penetration of lithium ions into the interior of the plates. This unique architecture determines specificity of the material interaction with lithium ions.

Most researchers hold the view that the electrochemical interaction of MoS₂ with lithium ions is irreversible at the potentials below 1.1 V^{1,20}. The products of this interaction are metallic molybdenum and lithium sulfide (reaction (2) in Fig. 7a) and with the further operation of the battery, its capacity is provided by reversible processes in the Li-S system (reaction (3) in Fig. 7a). These redox processes occur in our materials at potentials of 1.9–2.1 and 2.3–2.6 V (Fig. 6 a–d). The large area of the corresponding peaks in the CV curves indicates that these processes dominate. Moreover, their contribution to the material capacity increases with the scan rate of potential (Fig. 6e). The voltage plateau of nanostructured MoS₂ materials is 1.2–1.5 V. A

combination of such anode materials with suitable cathode materials is a promising approach for assembling of high-voltage full batteries ⁶⁶.

The CV curves of nanostructured MoS₂ showed three additional peaks at lower potentials, which are identified even after 60 full cycles of battery operation. (Fig. 6 a–e). According to the literature, the pair of peaks R2/O2 recorded at 1.19/1.7 V for ATM700 sample corresponds to the reversible intercalation of lithium between MoS₂ layers (reaction (1) in Fig. 7 (a)) ^{26,67}. The preservation of MoS₂ layers in the electrode material is confirmed by ex situ XRD studies showing the presence of (002) MoS₂ reflection after several full discharge-charge cycles (Fig. 5). The distance between the layers increased to ~1 nm, which, according to the results of ab initio calculations, corresponds to 2–3 lithium atoms per MoS₂ structural unit²⁰. The corresponding redox pair is often fixed on the CV curves of the composites of MoS₂ with graphene ^{64,68,69}. Strong MoS₂–graphene contacts can stabilize the structure of MoS₂ layers even after hundreds of discharge-charge cycles ²⁶. In our case, the surface carbon coating can prevent the destruction of the underlying MoS₂ layers and save the integrity of the plates during the battery operation observed by the SEM examination of electrode material (Fig. S10). Preservation of the structure of the layers in the inner part of the plates can be ensured by sulfur compounds formed in the expanded interlayer space and acting as a glue for neighboring layers. A study of the kinetics of the processes corresponding to the R2 and O2 peaks showed the presence of a capacitive contribution along with the predominant diffusion (Fig. 6f). The redox reaction, in this case, could be associated with the interaction of lithium ions with intercalated sulfur. The R3 peak that appears at 0.41 V in the CV curves of ATM700 material can be attributed to the reaction of molybdenum clusters with lithium ions to form Mo/Li_y ⁶¹. The lack of a clear oxidation peak for such a reaction may be due to the synthesis of compounds of different compositions ¹⁷.

Based on the above arguments, the structure of the material after several tens of intercalation/deintercalation cycles by lithium ions can be represented as a composite consisting of expanded MoS₂ nanosheets, elemental sulfur and molybdenum clusters (Fig. 7b). The

composite is surrounded by an outer carbon shell contacting the underlying MoS₂ layers. Defects in this environment allow lithium ions to penetrate the composite, however, they limit the diffusion of lithium polysulfides, which ensures the stability of the battery at current densities up to 2 A g⁻¹ inclusive (Fig. 4f). The EIS data for ATM700 material revealed a high diffusion rate of lithium ions and a low contact resistance of charge transfer (Fig. 4e). The first factor can be associated with a uniform distribution of sulfur over the volume of the composite, and the second can be determined by the presence of molybdenum clusters and Mo-terminated MoS₂ nanolayers, which ensure the electrical conductivity of the material^{18,59}. Such porous structure remains stable during long cycling at a current density 0.5 mAh g⁻¹ (Fig.7c). The sample does not lose the capacity for at least 60 cycles, whose value reaches 840 mAh g⁻¹.

4. Conclusion

Porous nanostructured MoS₂ was synthesized in non-equilibrium conditions created due to the thermal shock of fine-dispersed (NH₄)₂MoS₄. TG analysis of the precursor revealed that the formation of MoS₂ occurs around 400 °C and at 700 °C the evolution of gaseous decomposition products ends. These two temperatures were chosen as the boundaries of the temperature range during synthesis. According to electron microscopy, the obtained materials are elongated thin plates with many nanoscale pores, formed by intertwined curved MoS₂ layers. The number of layers and their lateral size increase with the synthesis temperature as the XRD data showed. The reversible specific capacity of MoS₂ materials in lithium-ion half-cells reached more than 800 mAh g⁻¹ at a current density of 0.1 A g⁻¹. The material synthesized at 700 °C showed the best rate capabilities and was able to deliver 817 mAh g⁻¹ at 2 A g⁻¹ and 1139 mAh g⁻¹ with subsequent cell cycling at 0.1 A g⁻¹. Long-term cycling revealed the stability of this material during at least 60 consecutive insertion/extraction of lithium ions at a current density of 0.5 A g⁻¹. The hierarchical porous structure of the material with a rigid outer shell containing edge defects provides rapid diffusion of lithium ions and prevents the loss of active sulfur species from the electrode. The proposed method can be implemented to synthesize chalcogenides of redox-active

metals and the resulting porous nanostructured materials could be interesting for various energy applications including alkali-metal-ion batteries.

Acknowledgments

We thank Dr. B. A. Kolesov for the Raman spectra, Dr. A.V. Ishchenko for the TEM data, the ICT SB RAS for access to XPS and the BIC SB RAS for BET surface measurement. The work was conducted under financial support of the Russian Science Foundation (Grant 16-13-0016).

Supporting information

IR-spectrum of $(\text{NH}_4)_2\text{MoS}_4$ aerogel. Details for TG and DSC curves for ATM aerogel. SEM images of the synthesis products. Pore size distribution in ATM600. Survey, Mo 3d and C 1s XPS spectra of samples and atomic contents of elements determined from XPS and CHNS analysis. High-frequency impedance spectra. Discharge-charge curves at 40th cycle of the batteries. Electrochemical performance of ATM800 sample. SEM images of electrode materials.

References

- (1) Stephenson, T.; Li, Z.; Olsen B.; Mitlin, D. Lithium Ion Battery Applications of Molybdenum Disulfide (MoS_2) Nanocomposites. *Energy Environ. Sci.* **2014**, *7*, 209. <https://doi.org/10.1039/c3ee42591f>.
- (2) Higashimoto, K.; Homma, H.; Uemura, Y.; Kawai, H.; Saibara, S.; Kensuke, H. Automotive Lithium-Ion Batteries. *Hitachi Rev.* **2011**, *60* (1), 17–21.
- (3) Demirocak, D. E.; Srinivasan, S. S.; Stefanakos, E. K. A Review on Nanocomposite Materials for Rechargeable Li-Ion Batteries. *Appl. Sci.* **2017**, *7* (7), 1–26. <https://doi.org/10.3390/app7070731>.
- (4) Gandoman, F. H.; Jaguemont, J.; Goutam, S.; Gopalakrishnan, R.; Firouz, Y.; Kalogiannis, T.; Omar, N.; Van Mierlo, J. Concept of Reliability and Safety Assessment of Lithium-Ion Batteries in Electric Vehicles: Basics, Progress, and Challenges. *Appl. Energy* **2019**, *251* (April), 113343. <https://doi.org/10.1016/j.apenergy.2019.113343>.
- (5) Saritha, D. A Concise Review on the Advancement of Anode Materials for Li-Ion Batteries. *Mater. Today Proc.* **2019**, *19*, 726–730. <https://doi.org/10.1016/j.matpr.2019.07.759>.
- (6) Roselin, L. S.; Juang, R. S.; Hsieh, C. Te; Sagadevan, S.; Umar, A.; Selvin, R.; Hegazy, H. H. Recent Advances and Perspectives of Carbon-Based Nanostructures as Anode Materials for Li-Ion Batteries. *Materials (Basel)*. **2019**, *12* (8). <https://doi.org/10.3390/ma12081229>.
- (7) Thanh, T. D.; Chuong, N. D.; Hien, H. Van; Kshetri, T.; Tuan, L. H.; Kim, N. H.; Lee, J. H. Recent Advances in Two-Dimensional Transition Metal Dichalcogenides-Graphene

- Heterostructured Materials for Electrochemical Applications. *Prog. Mater. Sci.* **2018**, *96*, 51–85. <https://doi.org/10.1016/j.pmatsci.2018.03.007>.
- (8) Zhu, Z.; Tang, Y.; Leow, W. R.; Xia, H.; Lv, Z.; Wei, J.; Ge, X.; Cao, S.; Zhang, Y.; Zhang, W.; Zhang, H.; Xi, S.; Du, Y.; Chen, X. Approaching the Lithiation Limit of MoS₂ While Maintaining Its Layered Crystalline Structure to Improve Lithium Storage. *Angew. Chemie - Int. Ed.* **2019**, *58* (11), 3521–3526. <https://doi.org/10.1002/anie.201813698>.
- (9) Enyashin, A. N.; Seifert, G. Density-Functional Study of Li_xMoS₂ Intercalates (0 ≤ x ≤ 1). *Comput. Theor. Chem.* **2012**, *999* (343), 13–20. <https://doi.org/http://dx.doi.org/10.1016/j.comptc.2012.08.005>.
- (10) Wang, Z.; Chen, T.; Chen, W.; Chang, K.; Ma, L.; Huang, G.; Chen, D.; Lee, J. Y. CTAB-Assisted Synthesis of Single-Layer MoS₂-Graphene Composites as Anode Materials of Li-Ion Batteries. *J. Mater. Chem. A* **2013**, *1* (6), 2202. <https://doi.org/10.1039/c2ta00598k>.
- (11) Chang, K.; Chen, W. In Situ Synthesis of MoS₂/Graphene Nanosheet Composites with Extraordinarily High Electrochemical Performance for Lithium Ion Batteries. *Chem. Commun.* **2011**, *47* (14), 4252. <https://doi.org/10.1039/c1cc10631g>.
- (12) Stolyarova, S. G.; Koroteev, V. O.; Shubin, Y. V.; Plyusnin, P. E.; Makarova, A. A.; Okotrub, A. V.; Bulusheva, L. G. Pressure-Assisted Interface Engineering in MoS₂/Holey Graphene Hybrids for Improved Performance in Li-Ion Batteries. *Energy Technol.* **2019**, *7* (10), 1–11. <https://doi.org/10.1002/ente.201900659>.
- (13) Du, G.; Guo, Z.; Wang, S.; Zeng, R.; Chen, Z.; Liu, H. Superior Stability and High Capacity of Restacked Molybdenum Disulfide as Anode Material for Lithium Ion Batteries. *Chem. Commun.* **2010**, *46* (7), 1106–1108. <https://doi.org/10.1039/b920277c>.
- (14) Dumcenco, D.; Ovchinnikov, D.; Marinov, K.; Lazić, P.; Gibertini, M.; Marzari, N.; Sanchez, O. L.; Kung, Y. C.; Krasnozhan, D.; Chen, M. W.; Bertolazzi, S.; Gillet, P.; Fontcuberta I Morral, A.; Radenovic, A.; Kis, A. Large-Area Epitaxial Monolayer MoS₂. *ACS Nano* **2015**, *9* (4), 4611–4620. <https://doi.org/10.1021/acsnano.5b01281>.
- (15) Guo, Y.-G.; Hu, J.-S.; Wan, L.-J. Nanostructured Materials for Electrochemical Energy Conversion and Storage Devices. *Adv. Mater.* **2008**, *20* (15), 2878–2887. <https://doi.org/10.1002/adma.200800627>.
- (16) Liu, Q.; Weijun, X.; Wu, Z.; Huo, J.; Liu, D.; Wang, Q.; Wang, S. The Origin of the Enhanced Performance of Nitrogen-Doped MoS₂ in Lithium Ion Batteries. *Nanotechnology* **2016**, *27* (17). <https://doi.org/10.1088/0957-4484/27/17/175402>.
- (17) Wang, L.; Zhang, Q.; Zhu, J.; Duan, X.; Xu, Z.; Liu, Y.; Yang, H.; Lu, B. Nature of Extra Capacity in MoS₂ Electrodes: Molybdenum Atoms Accommodate with Lithium. *Energy Storage Mater.* **2019**, *16* (March 2018), 37–45. <https://doi.org/10.1016/j.ensm.2018.04.025>.
- (18) Wang, M.; Xu, Y. H.; Lu, F.; Zhu, Z.; Dong, J. Y.; Fang, D. L.; Zhou, J.; Yang, Y. J.; Zhong, Y. T.; Chen, S. M.; Bando, Y.; Golberg, D.; Wang, X. Enhanced Li-Ion-Storage Performance of MoS₂ through Multistage Structural Design. *ChemElectroChem* **2019**, *6* (5), 1475–1484. <https://doi.org/10.1002/celec.201801533>.
- (19) Jiang, F.; Li, S.; Ge, P.; Tang, H.; Khoso, S. A.; Zhang, C.; Yang, Y.; Hou, H.; Hu, Y.; Sun, W.; Ji, X. Size-Tunable Natural Mineral-Molybdenite for Lithium-Ion Batteries toward: Enhanced Storage Capacity and Quicken Ions Transferring. *Front. Chem.* **2018**, *6*

- (AUG), 1–12. <https://doi.org/10.3389/fchem.2018.00389>.
- (20) Sen, U. K.; Johari, P.; Basu, S.; Nayak, C.; Mitra, S. An Experimental and Computational Study to Understand the Lithium Storage Mechanism in Molybdenum Disulfide. *Nanoscale* **2014**, *6* (17), 10243–10254. <https://doi.org/10.1039/c4nr02480j>.
- (21) Zhang, L.; Sun, D.; Kang, J.; Feng, J.; Bechtel, H. A.; Wang, L. W.; Cairns, E. J.; Guo, J. Electrochemical Reaction Mechanism of the MoS₂ Electrode in a Lithium-Ion Cell Revealed by in Situ and Operando X-Ray Absorption Spectroscopy. *Nano Lett.* **2018**, *18* (2), 1466–1475. <https://doi.org/10.1021/acs.nanolett.7b05246>.
- (22) Manthiram, A.; Fu, Y.; Chung, S. H.; Zu, C.; Su, Y. S. Rechargeable Lithium-Sulfur Batteries. *Chem. Rev.* **2014**, *114* (23), 11751–11787. <https://doi.org/10.1021/cr500062v>.
- (23) Bulusheva, L. G.; Koroteev, V. O.; Stolyarova, S. G.; Chuvilin, A. L.; Plyusnin, P. E.; Shubin, Y. V.; Vilkov, O. Y.; Chen, X.; Song, H.; Okotrub, A. V. Effect of In-Plane Size of MoS₂ Nanoparticles Grown over Multilayer Graphene on the Electrochemical Performance of Anodes in Li-Ion Batteries. *Electrochim. Acta* **2018**, *283*, 45. <https://doi.org/10.1016/j.electacta.2018.06.134>.
- (24) Su, Q.; Wang, S.; Feng, M.; Du, G.; Xu, B. Direct Studies on the Lithium-Storage Mechanism of Molybdenum Disulfide. *Sci. Rep.* **2017**, *7* (1), 7275. <https://doi.org/10.1038/s41598-017-07648-0>.
- (25) Li, X.; Zai, J.; Xiang, S.; Liu, Y.; He, X.; Xu, Z.; Wang, K.; Ma, Z.; Qian, X. Regeneration of Metal Sulfides in the Delithiation Process: The Key to Cyclic Stability. *Adv. Energy Mater.* **2016**, *6* (19), 1–8. <https://doi.org/10.1002/aenm.201601056>.
- (26) Chen, B.; Meng, Y.; He, F.; Liu, E.; Shi, C.; He, C.; Ma, L.; Li, Q.; Li, J.; Zhao, N. Thermal Decomposition-Reduced Layer-by-Layer Nitrogen-Doped Graphene/MoS₂/Nitrogen-Doped Graphene Heterostructure for Promising Lithium-Ion Batteries. *Nano Energy* **2017**, *41* (July), 154–163. <https://doi.org/10.1016/j.nanoen.2017.09.027>.
- (27) Shokhen, V.; Miroshnikov, Y.; Gershinsky, G.; Gotlib, N.; Stern, C.; Naveh, D.; Zitoun, D. On the Impact of Vertical Alignment of MoS₂ for Efficient Lithium Storage. *Sci. Rep.* **2017**, *7* (1), 1–11. <https://doi.org/10.1038/s41598-017-03453-x>.
- (28) Jiao, Y.; Mukhopadhyay, A.; Ma, Y.; Yang, L.; Hafez, A. M.; Zhu, H. Ion Transport Nanotube Assembled with Vertically Aligned Metallic MoS₂ for High Rate Lithium-Ion Batteries. *Adv. Energy Mater.* **2018**, *8* (15), 1–9. <https://doi.org/10.1002/aenm.201702779>.
- (29) Zhang, Z.; Wu, S.; Cheng, J.; Zhang, W. MoS₂ Nanobelts with (002) Plane Edges-Enriched Flat Surfaces for High-Rate Sodium and Lithium Storage. *Energy Storage Mater.* **2018**, *15* (002), 65–74. <https://doi.org/10.1016/j.ensm.2018.03.013>.
- (30) Liu, H.; Su, D.; Zhou, R.; Sun, B.; Wang, G.; Qiao, S. Z. Highly Ordered Mesoporous MoS₂ with Expanded Spacing of the (002) Crystal Plane for Ultrafast Lithium Ion Storage. *Adv. Energy Mater.* **2012**, *2* (8), 970–975. <https://doi.org/10.1002/aenm.201200087>.
- (31) Wang, M.; Li, G.; Xu, H.; Qian, Y.; Yang, J. Enhanced Lithium Storage Performances of Hierarchical Hollow MoS₂ Nanoparticles Assembled from Nanosheets. *ACS Appl. Mater. Interfaces* **2013**, *5* (3), 1003–1008. <https://doi.org/10.1021/am3026954>.
- (32) Kaniyoor, A.; Baby, T. T.; Ramaprabhu, S. Graphene Synthesis via Hydrogen Induced Low Temperature Exfoliation of Graphite Oxide. *J. Mater. Chem.* **2010**, *20* (39), 8467–8469. <https://doi.org/10.1039/c0jm01876g>.

- (33) Qiao, Y.; Liu, Y.; Chen, C.; Xie, H.; Yao, Y.; He, S.; Ping, W.; Liu, B.; Hu, L. 3D-Printed Graphene Oxide Framework with Thermal Shock Synthesized Nanoparticles for Li-CO₂ Batteries. *Adv. Funct. Mater.* **2018**, *28* (51), 1–7. <https://doi.org/10.1002/adfm.201805899>.
- (34) Bai, L. Z.; Zhao, D. L.; Zhang, T. M.; Xie, W. G.; Zhang, J. M.; Shen, Z. M. A Comparative Study of Electrochemical Performance of Graphene Sheets, Expanded Graphite and Natural Graphite as Anode Materials for Lithium-Ion Batteries. *Electrochim. Acta* **2013**, *107*, 555. <https://doi.org/10.1016/j.electacta.2013.06.032>.
- (35) Li, Q.; Guo, X.; Zhang, Y.; Zhang, W.; Ge, C.; Zhao, L.; Wang, X.; Zhang, H.; Chen, J.; Wang, Z.; Sun, L. Porous Graphene Paper for Supercapacitor Applications. *J. Mater. Sci. Technol.* **2017**. <https://doi.org/10.1016/j.jmst.2017.03.018>.
- (36) Sysoev, V. I.; Bulusheva, L. G.; Asanov, I. P.; Shubin, Y. V.; Okotrub, A. V. Thermally Exfoliated Fluorinated Graphite for NO₂ Gas Sensing. *Phys. Status Solidi Basic Res.* **2016**, *253* (12), 2492–2498. <https://doi.org/10.1002/pssb.201600270>.
- (37) Wang, H. W.; Skeldon, P.; Thompson, G. E.; Wood, G. C. Synthesis and Characterization of Molybdenum Disulphide Formed from Ammonium Tetrathiomolybdate. *J. Mater. Sci.* **1997**, *32* (2), 497–502. <https://doi.org/10.1023/A:1018538424373>.
- (38) Lin, C. H.; Tsai, C. H.; Tseng, F. G.; Yu, Y. Y.; Wu, H. C.; Hsieh, C. K. Low-Temperature Thermally Reduced Molybdenum Disulfide as a Pt-Free Counter Electrode for Dye-Sensitized Solar Cells. *Nanoscale Res. Lett.* **2015**, *10* (1), 1–10. <https://doi.org/10.1186/s11671-015-1156-0>.
- (39) NETZSCH-Gerätebau GmbH-Selb/Bayern. NETZSCH Proteus Thermal Analysis v.6.1.0. **2013**.
- (40) Zhang, J.; Hu, S.; Feng, Y.; Xu, B.; Guo, Y. Synthesis and Characterization of Rodlike Ammonium Tetrathiomolybdate and Its Thermal Decomposition Mechanism. *Adv. Mater. Res.* **2011**, *287–290*, 2049–2052. <https://doi.org/10.4028/www.scientific.net/AMR.287-290.2049>.
- (41) Chen, D.; Liu, M.; Yin, L.; Li, T.; Yang, Z.; Li, X.; Fan, B.; Wang, H.; Zhang, R.; Li, Z.; Xu, H.; Lu, H.; Yang, D.; Sun, J.; Gao, L. Single-Crystalline MoO₃ Nanoplates: Topochemical Synthesis and Enhanced Ethanol-Sensing Performance. *J. Mater. Chem.* **2011**, *21* (25), 9332–9342. <https://doi.org/10.1039/c1jm11447f>.
- (42) Peng, Y. Y.; Liu, Y. M.; Chang, J. K.; Wu, C. H.; Ger, M. Der; Pu, N. W.; Chang, C. L. A Facile Approach to Produce Holey Graphene and Its Application in Supercapacitors. *Adv. Funct. Mater.* **2015**, *81* (19), 2920–2927. <https://doi.org/10.1002/adfm.201500321>.
- (43) Wang, H. W.; Skeldon, P.; Thompson, G. E. Thermogravimetric-Differential Thermal Analysis of the Solid-State Decomposition of Ammonium Tetrathiomolybdate during Heating in Argon. *J. Mater. Sci.* **1998**, *33* (12), 3079–3083. <https://doi.org/10.1023/A:1004335604327>.
- (44) Brito, J. L.; Ilija, M.; Hernández, P. Thermal and Reductive Decomposition of Ammonium Thiomolybdates. *Thermochim. Acta* **1995**, *256* (2), 325–338. [https://doi.org/10.1016/0040-6031\(94\)02178-Q](https://doi.org/10.1016/0040-6031(94)02178-Q).
- (45) Wang, H. W.; Skeldon, P.; Thompson, G. E.; Wood, G. C. Synthesis and Characterization of Molybdenum Disulphide Formed from Ammonium Tetrathiomolybdate. *J. Mater. Sci.* **1997**, *32* (2), 497–502. <https://doi.org/10.1023/A:1018538424373>.
- (46) Lee, C.; Yan, H.; Brus, L. E.; Heinz, T. F.; Hone, J.; Ryu, S. Anomalous Lattice Vibrations of Single and Few-Layer MoS₂. *ACS Nano* **2010**, *4* (5), 2695.

<https://doi.org/10.1021/nm1003937>.

- (47) Zhang, X.; Qiao, X. F.; Shi, W.; Wu, J. Bin; Jiang, D. S.; Tan, P. H. Phonon and Raman Scattering of Two-Dimensional Transition Metal Dichalcogenides from Monolayer, Multilayer to Bulk Material. *Chem. Soc. Rev.* **2015**, *44* (9), 2757–2785. <https://doi.org/10.1039/c4cs00282b>.
- (48) Li, H.; Zhang, Q.; Yap, C. C. R.; Tay, B. K.; Edwin, T. H. T.; Olivier, A.; Baillargeat, D. From Bulk to Monolayer MoS₂: Evolution of Raman Scattering. *Adv. Funct. Mater.* **2012**, *22* (7), 1385–1390. <https://doi.org/10.1002/adfm.201102111>.
- (49) Blanco, É.; Afanasiev, P.; Berhault, G.; Uzio, D.; Loricant, S. Resonance Raman Spectroscopy as a Probe of the Crystallite Size of MoS₂ Nanoparticles. *Comptes Rendus Chim.* **2016**, *19* (10), 1310–1314. <https://doi.org/10.1016/j.crci.2015.08.014>.
- (50) Koroteev, V. O.; Bulushev, D. A.; Chuvilin, A. L.; Okotrub, A. V.; Bulusheva, L. G. Nanometer-Sized MoS₂ Clusters on Graphene Flakes for Catalytic Formic Acid Decomposition. *ACS Catal.* **2014**, *4* (11), 3950. <https://doi.org/10.1021/cs500943b>.
- (51) Peisert, H.; Chassé, T.; Streubel, P.; Meisel, A.; Szargan, R. Relaxation Energies in XPS and XAES of Solid Sulfur Compounds. *J. Electron Spectros. Relat. Phenomena* **1994**, *68*, 321–328. [https://doi.org/10.1016/0368-2048\(94\)02129-5](https://doi.org/10.1016/0368-2048(94)02129-5).
- (52) Smart, R. S. C.; Skinner, W. M.; Gerson, A. R. XPS of Sulphide Mineral Surfaces : Metal-Deficient , Polysulphides , Defects and Elemental Sulphur. *Surf. interface Anal.* **1999**, *105* (November 1998), 101–105.
- (53) Stolyarova, S. G.; Koroteev, V. O.; Baskakova, K. I.; Makarova, A. A.; Okotrub, A. V.; Bulusheva, L. G. Anode Materials from MoS₂ and Multilayered Holey Graphene for Li-Ion Batteries. *Fullerenes Nanotub. Carbon Nanostructures* **2020**, *28* (4), 328–334. <https://doi.org/10.1080/1536383X.2019.1708735>.
- (54) Butenko, Y. V.; Krishnamurthy, S.; Chakraborty, A. K.; Kuznetsov, V. L.; Dhanak, V. R.; Hunt, M. R. C.; Šiller, L. Photoemission Study of Onionlike Carbons Produced by Annealing Nanodiamonds. *Phys. Rev. B - Condens. Matter Mater. Phys.* **2005**, *71* (7), 1–10. <https://doi.org/10.1103/PhysRevB.71.075420>.
- (55) Fedoseeva, Y. V.; Pozdnyakov, G. A.; Okotrub, A. V.; Kanygin, M. A.; Nastaushev, Y. V.; Vilkov, O. Y.; Bulusheva, L. G. Effect of Substrate Temperature on the Structure of Amorphous Oxygenated Hydrocarbon Films Grown with a Pulsed Supersonic Methane Plasma Flow. *Appl. Surf. Sci.* **2016**, *385*, 464–471. <https://doi.org/10.1016/j.apsusc.2016.05.120>.
- (56) Stolyarova, S. G.; Kanygin, M. A.; Koroteev, V. O.; Shubin, Y. V.; Smirnov, D. A.; Okotrub, A. V.; Bulusheva, L. G. High-Pressure High-Temperature Synthesis of MoS₂/Holey Graphene Hybrids and Their Performance in Li-Ion Batteries. *Phys. Status Solidi Basic Res.* **2018**, *255* (1), 1700262. <https://doi.org/10.1002/pssb.201700262>.
- (57) Blume, R.; Rosenthal, D.; Tessonier, J. P.; Li, H.; Knop-Gericke, A.; Schlögl, R. Characterizing Graphitic Carbon with X-Ray Photoelectron Spectroscopy: A Step-by-Step Approach. *ChemCatChem* **2015**, *7* (18), 2871–2881. <https://doi.org/10.1002/cctc.201500344>.
- (58) Kumar, R. V.; Sarakonsri, T. Introduction to Electrochemical Cells. In *High Energy Density Lithium Batteries*; Katerina, E. A., Hackney, S. A., Kumar, R. V., Eds.; WILEY-VCH Verlag GmbH & Co.: Weinheim, 2012; Vol. 216, pp 48–51. <https://doi.org/10.1016/j.rser.2013.08.001>.

- (59) Chen, Q.; Li, H.; Xu, W.; Wang, S.; Sawada, H.; Allen, C. S.; Kirkland, A. I.; Grossman, J. C.; Warner, J. H. Atomically Flat Zigzag Edges in Monolayer MoS₂ by Thermal Annealing. *Nano Lett.* **2017**, *17* (9), 5502–5507. <https://doi.org/10.1021/acs.nanolett.7b02192>.
- (60) Abraham, A.; Wang, L.; Quilty, C. D.; Lutz, D. M.; McCarthy, A. H.; Tang, C. R.; Dunkin, M. R.; Housel, L. M.; Takeuchi, E. S.; Marschilok, A. C.; Takeuchi, K. J. Defect Control in the Synthesis of 2 D MoS₂ Nanosheets: Polysulfide Trapping in Composite Sulfur Cathodes for Li–S Batteries. *ChemSusChem* **2020**, *13* (6), 1517–1528. <https://doi.org/10.1002/cssc.201903028>.
- (61) Xiao, J.; Wang, X.; Yang, X. Q.; Xun, S.; Liu, G.; Koech, P. K.; Liu, J.; Lemmon, J. P. Electrochemically Induced High Capacity Displacement Reaction of PEO/MoS₂/Graphene Nanocomposites with Lithium. *Adv. Funct. Mater.* **2011**, *21* (15), 2840–2846. <https://doi.org/10.1002/adfm.201002752>.
- (62) Zhou, F.; Xin, S.; Liang, H. W.; Song, L. T.; Yu, S. H. Carbon Nanofibers Decorated with Molybdenum Disulfide Nanosheets: Synergistic Lithium Storage and Enhanced Electrochemical Performance. *Angew. Chemie - Int. Ed.* **2014**, *53* (43), 11552–11556. <https://doi.org/10.1002/anie.201407103>.
- (63) Chang, U.; Lee, J. T.; Yun, J. M.; Lee, B.; Lee, S. W.; Joh, H. I.; Eom, K.; Fuller, T. F. In Situ Self-Formed Nanosheet MoS₃/Reduced Graphene Oxide Material Showing Superior Performance as a Lithium-Ion Battery Cathode. *ACS Nano* **2019**, *13* (2), 1490–1498. <https://doi.org/10.1021/acsnano.8b07191>.
- (64) Wang, T.; Xu, Z.; Yang, J.; Liu, X.; Cheng, Y.; Li, J.; Shen, X.; Huang, J. Tailoring MoS₂ Ultrathin Sheets Anchored on Graphene Flexible Supports for Superstable Lithium-Ion Battery Anodes. *Part. Part. Syst. Charact.* **2019**, *36* (9), 1–9. <https://doi.org/10.1002/ppsc.201900197>.
- (65) Bard, A. J.; Faulkner, L. R. *Electrochemical Methods. Fundamentals and Applications*, Second ed.; Harris, D., Swain, E., Robey, C., Aiello, E., Eds.; JOHN WILEY & SONS, INC: New York, Chichester • Weinheim, Brisbane e Singapore e Toronto, 2001; Vol. 677. <https://doi.org/10.1016/j.aca.2010.06.020>.
- (66) Lutz, J.; Schlangemotto, H.; Scheuermann, U.; Doncker, R. *Semiconductor Power Devices. Physics, Characteristics, Reliability*; Springer, 2011; Vol. 53. <https://doi.org/10.1017/CBO9781107415324.004>.
- (67) Fan, H.; Chen, X.; Tang, Q.; Chen, S.; Fan, B.; Hu, A.; Zhang, S.; Li, Y. Molybdenum Disulfide Nanosheet Embedded Three-Dimensional Vertically Aligned Carbon Nanotube Arrays for Extremely-Excellent Cycling Stability Lithium-Ion Anodes. *RSC Adv.* **2016**, *6* (83), 80320–80327. <https://doi.org/10.1039/c6ra17042k>.
- (68) Wang, G.; Zhang, J.; Yang, S.; Wang, F.; Zhuang, X.; Müllen, K.; Feng, X. Vertically Aligned MoS₂ Nanosheets Patterned on Electrochemically Exfoliated Graphene for High-Performance Lithium and Sodium Storage. *Adv. Energy Mater.* **2018**, *8* (8), 1–8. <https://doi.org/10.1002/aenm.201702254>.
- (69) Jing, L.; Lian, G.; Wang, J.; Zhao, M.; Liu, X.; Wang, Q.; Cui, D.; Wong, C. P. Porous-Hollow Nanorods Constructed from Alternate Intercalation of Carbon and MoS₂ Monolayers for Lithium and Sodium Storage. *Nano Res.* **2019**, *12* (8), 1912–1920. <https://doi.org/10.1007/s12274-019-2458-9>.

Table 1. Compositions of samples expected from the TG data of ATM

Temperature, °C	m*, %	composition
400	70.56	MoS _{2.6}
500	65.30	MoS _{2.1}
600	63.43	MoS _{2.0}
700	62.69	MoS _{1.9}

m* is the remaining weight of the sample at different temperatures.

Table 2. Structural parameters of the samples synthesized from ATM at 400, 500, 600, and 700 °C: d₀₀₂ and N_{layer} are the interlayer distance and the number of layers calculated from (002) reflection of MoS₂, Δ is the difference between the positions of E_{12g}¹ and A_{1g} peaks in Raman spectra.

Sample	d ₀₀₂ (Å)	N _{layer}	E _{12g} ¹ (cm ⁻¹)	A _{1g} (cm ⁻¹)	Δ (cm ⁻¹)
ATM400	6.4±0.2	2.8±0.2	378.3	402.1	23.8
ATM500	6.2±0.2	4.8±0.2	381.4	405.2	23.8
ATM600	6.3±0.2	5.2±0.2	379.3	403.1	23.8
ATM700	6.3±0.2	6.6±0.2	380.3	404.1	23.8

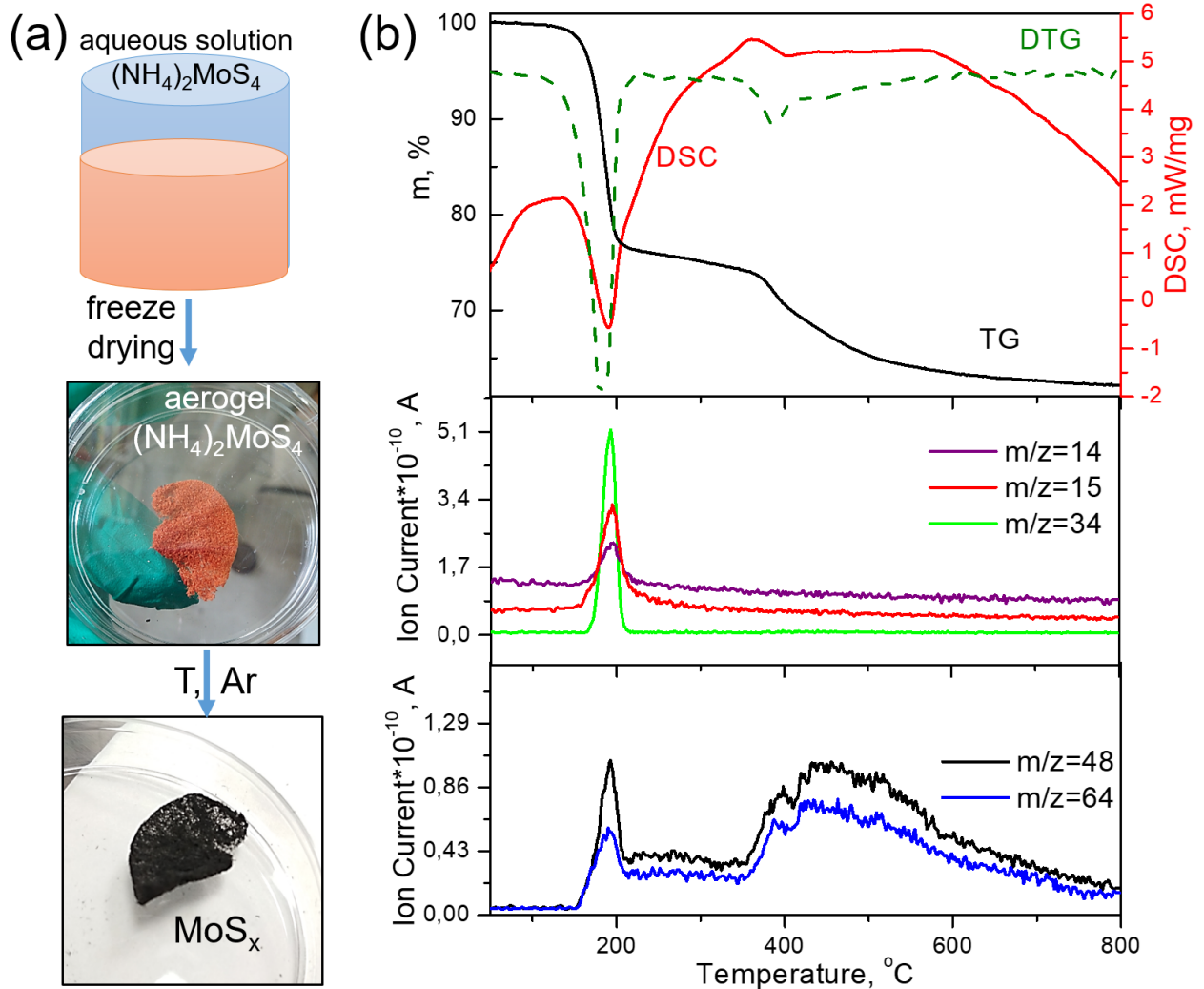


Fig. 1. Scheme of materials synthesis (a). TG, DTG, DSC (top), and ion current curves of evolved gases (bottom) measured for ATM aerogel (b).

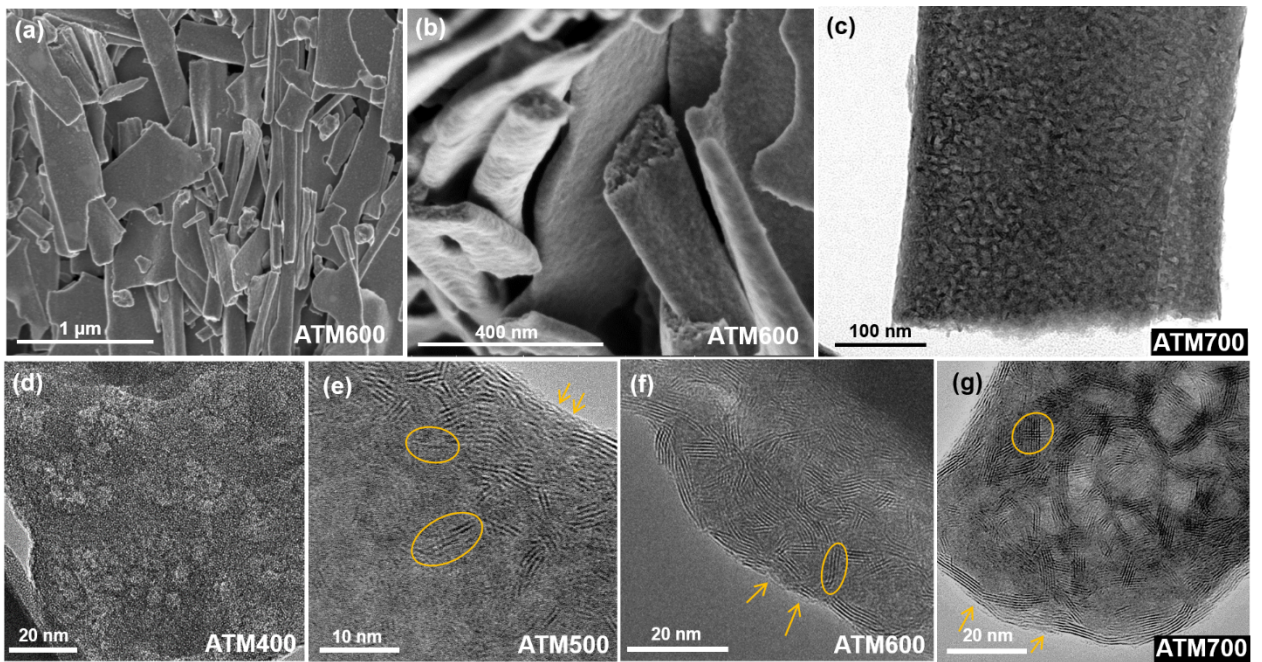


Fig. 2. SEM images (a, b) of ATM600 and low-resolution TEM images (c) ATM700 taken as illustration of typical morphology of the synthesis products. High-resolution TEM images of ATM400 (d), ATM500 (e), ATM600 (f), and ATM700 (g). The arrows show carbon on the surface of plates, the ovals show MoS₂ nanosheets.

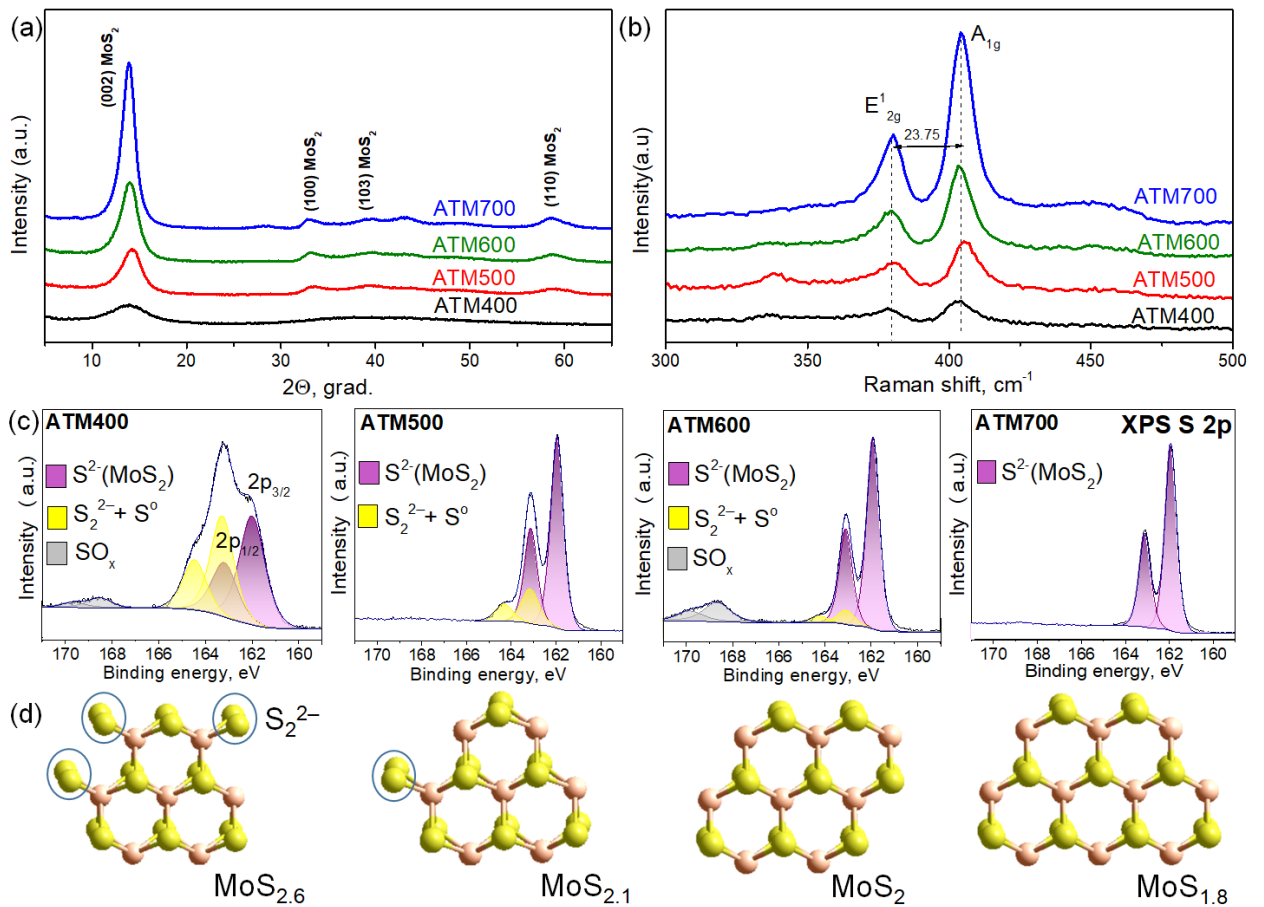


Fig. 3. XRD patterns (a), Raman spectra (b), and XPS S 2p spectra (c) of samples, obtained from ATM at synthesis temperatures 400°C (ATM400), 500°C (ATM500), 600°C (ATM600) and 700 °C (ATM700) and models of the structure of nanolayers (d) with the composition estimated from TG data (Table1).

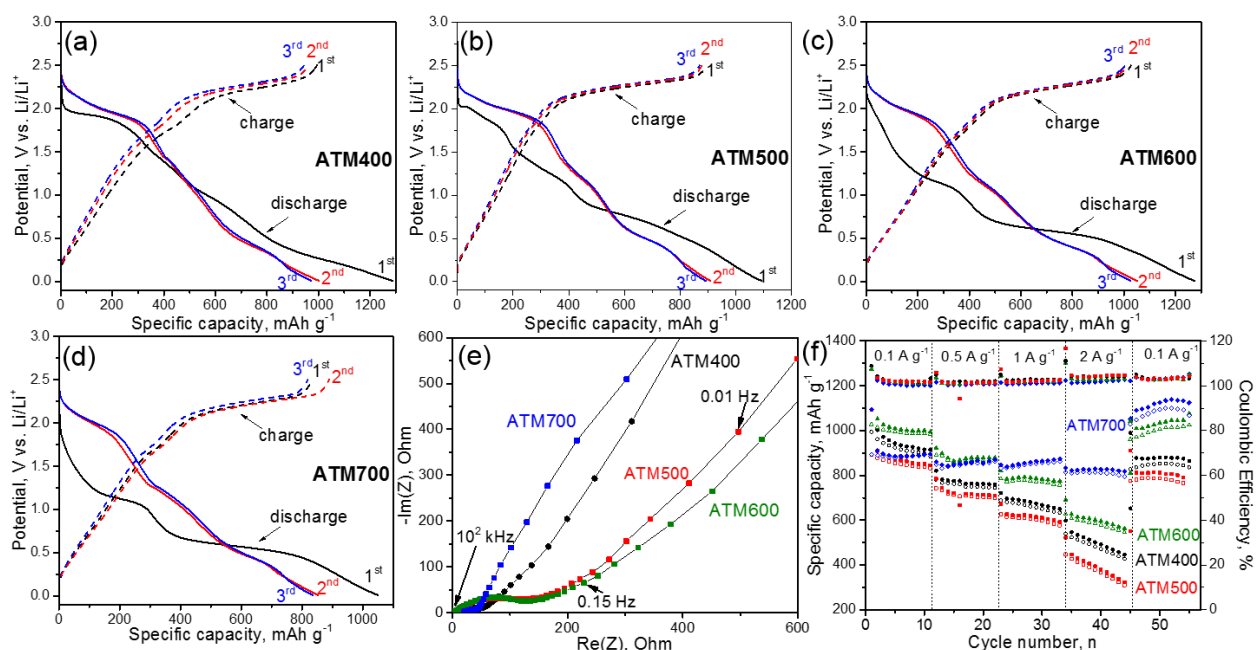


Fig.4. Initial three discharge-charge curves measured at current density of $0.1 \text{ A} \cdot \text{g}^{-1}$ for ATM400 (a), ATM500 (b), ATM600 (c), and ATM 700 (d). Nyquist plots (e) and rate capability (f) of studied samples.

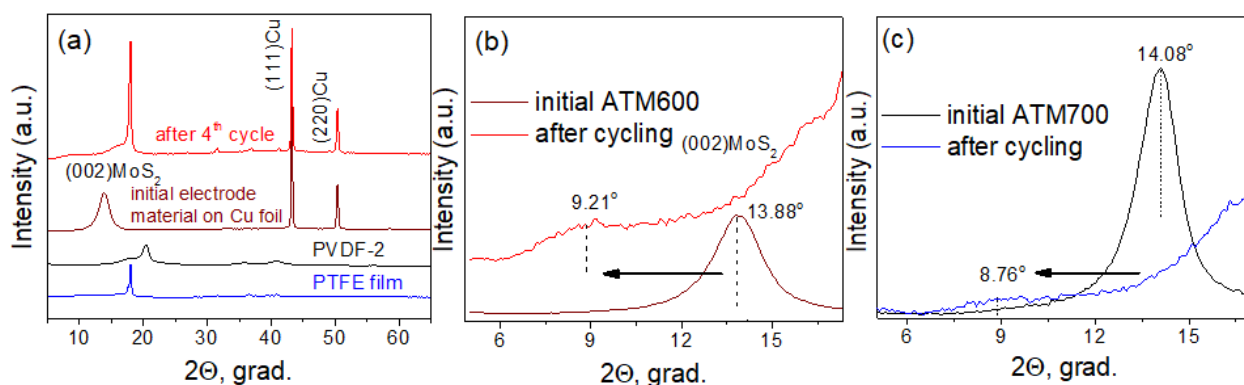


Fig. 5. XRD patterns of initial electrode material (ATM600 with PVDF-2 and super P) on copper foil and that after the four full discharge-charge cycles in comparison with the patterns of PVDF-2 binder and PTFE film (a). XRD patterns around (002) MoS_2 reflection for ATM600 (b) and ATM700 (c) before and after the fourth cycle.

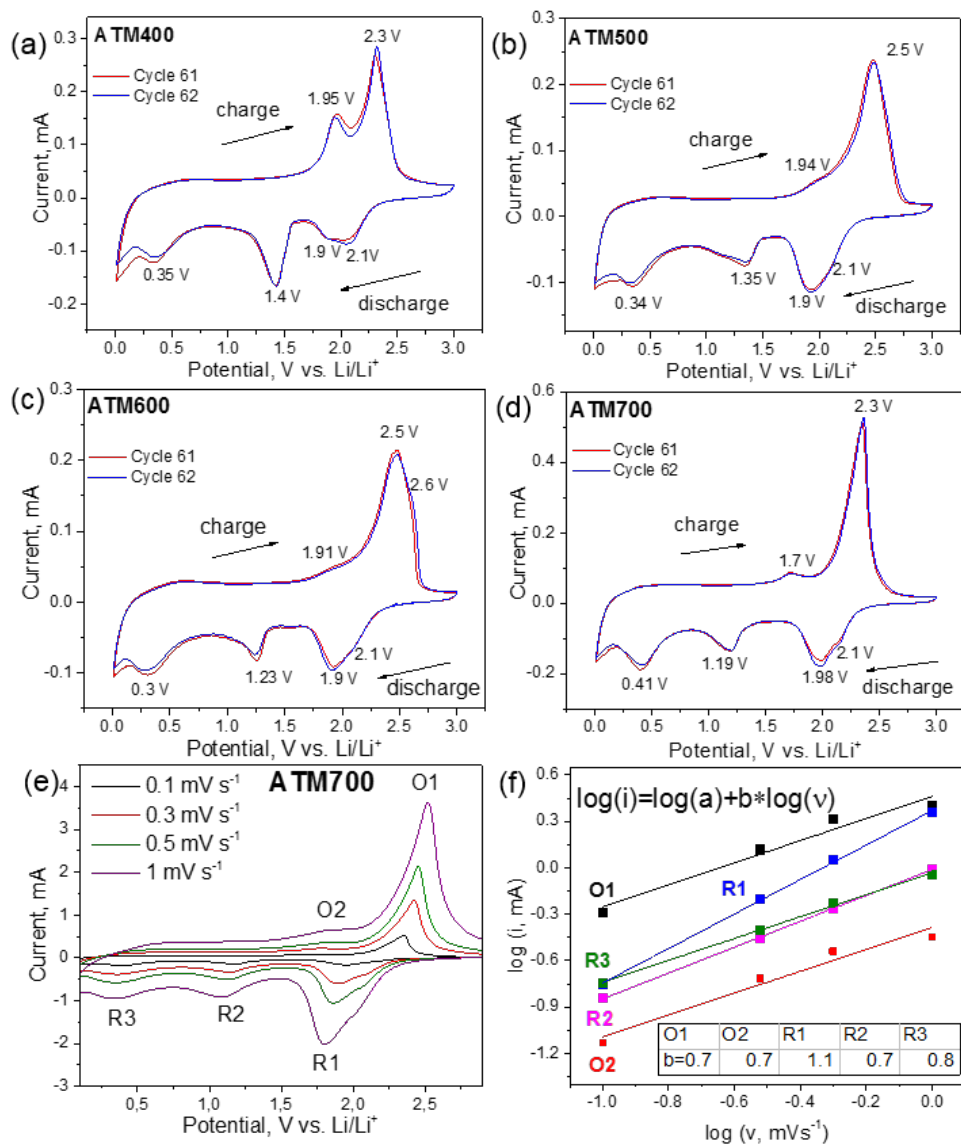


Fig. 6. CV curves measured in a voltage range of 0.01–3.0 V at a scan rate of 0.1 mVs⁻¹ for ATM400 (a), ATM500 (b), ATM600 (c) and ATM700 (d). CV curves for ATM700 sample taken at scan rates of 0.1–1 mV s⁻¹ (e). Dependences of log(*i*) vs. log(*v*) obtained for oxidation and reduction peaks observed for ATM700 (f).

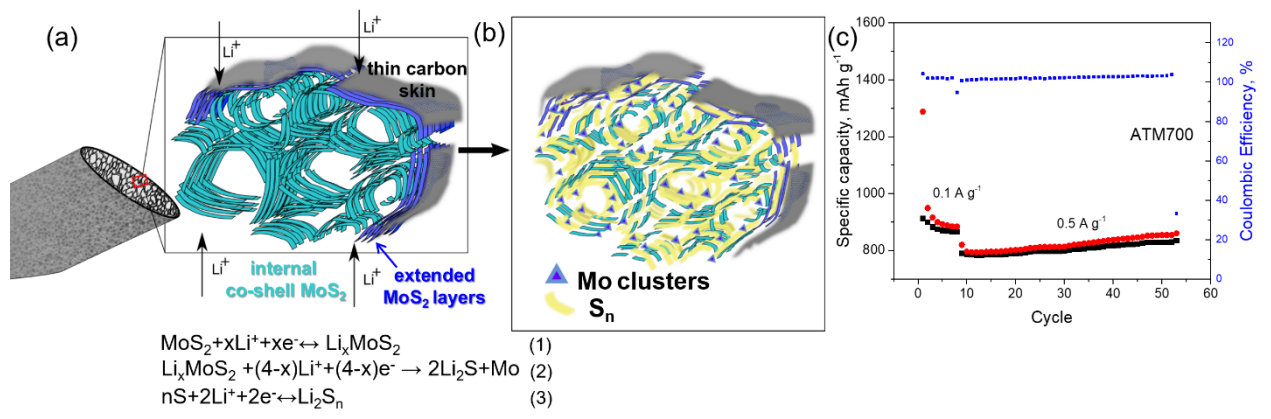


Fig. 7. Scheme of ATM700 material before (a) and after (b) reaction with lithium ions. Cycling performance of ATM700 sample at 0.1 and 0.5 A g^{-1} (c).

Graphical Table of Contents

